Journal of Fluids and Structures 17 (2003) 739–765

JOURNAL OF FLUIDS AND STRUCTURES

www.elsevier.nl/locate/jnlabr/yjfls

Computation of wind-induced vibrations of flexible shells and membranous structures

M. Glück[a,*], M. Breuer[a], F. Durst[a], A. Halfmann[b], E. Rank[b]

[a] *Institute of Fluid Mechanics, University of Erlangen-Nürnberg, Cauerstrasse 4, D-91058 Erlangen, Germany*
[b] *Institute of Computer Science in Civil Engineering, Technical University of Munich D-80290 München, Germany*

Received 19 December 2001; accepted 4 December 2002

Abstract

A partitioned coupling approach for time-dependent fluid–structure interactions is applied to thin shells and membranous structures with large displacements. The frame algorithm connects a three-dimensional, finite volume-based multi-block flow solver for incompressible fluids with a finite element code for geometrically nonlinear structural problems using a commercial coupling interface. Thus a high modularity is achieved and the whole range of opportunities with these two powerful codes — each of them highly adapted to its specific field of application — can be used also for coupled simulations.

Two completely different configurations were investigated. First, the coupling algorithm was applied to an academic test configuration consisting of one, two, and three flexible L-shaped plates being loaded by a steady far-field flow. Various investigations were carried out at different Reynolds numbers ($\mathrm{Re} = 50, 200$, and 500) in order to study phenomena such as vortex shedding, resonance, influence of the interaction between several flexible plates, whereas the second and third plates were placed in the wake of the first.

The second part of the paper shows that in principle the coupling procedure can also deal with real-life structures as they occur in civil engineering. A membranous roof of glass-fiber synthetics with a complex shape was exposed to a time-dependent wind gust from diagonally above which was superimposed on a constant basic wind flow parallel to the ground. The structural model contains the pre-stressed textile roof including the taut cables at its circumference which are fastened at the pylons. As a structural response, the wind gust led to a displacement of the textile roof which disappeared again when the gust subsided. With the coupled algorithm proposed in the paper it is possible to study dynamic interactions for engineering applications.

1. Introduction

Interaction phenomena between fluids and structures can be found in many engineering and also medical disciplines such as civil, mechanical and medical engineering, shipbuilding, and bio-medicine. Although the simulation tool presented in this paper was designed for *civil engineering* applications, it could also be applied to other fields.

Examples of the first-mentioned field of application include, in addition to suspension bridges, tall buildings, towers, off-shore platforms, and power lines, also *lightweight membranes* used as wide area roofage such as awnings, large umbrellas, and tent roofs. These structures are becoming more and more important, because architects prefer them in order to create unique masterpieces of design. Another crucial advantage is the efficient utilization of building material.

As an example, for the new roofage of the Gottlieb Daimler stadium in Stuttgart (Germany), it was decided in favor of a cable–membrane structure, which has an average weight of only 13 kg/m^2, whereas a cantilever roof with steel

*Corresponding author.
E-mail address: glueck@lstm.uni-erlangen.de (M. Glück).

0889-9746/03/$ - see front matter
doi:10.1016/S0889-9746(03)00006-9

skeleton framing, which was also possible, reached a dead load of 70–80 kg/m^2 (Bergermann et al., 1995). Accordingly, the supporting construction for the roof and the grounding required much less material. Thus membranous roofs are often not only the main creative element, but also a substantial part of the statics of the entire structure. One of the most spectacular buildings of this kind is the wired textile dome in Atlanta (USA), which canopies a stadium for 70,000 spectators with a span of 240 m.

To determine the wind loads of such buildings — especially for complex geometries or time-dependent external flows — expensive and time-consuming *experiments* in wind tunnels or *semi-empirical methods* are state-of-the-art. This work makes a contribution to establishing *numerical simulations* as an advantageous tool to predict the behavior of wind-loaded structures.

In principle, there are the following possibilities for fluid–structure interactions in buildings:

(i) The wind load on the structure causes a *steady deformation state*.
(ii) The fluid flow leads to a *time-dependent movement* of the structure, which is caused by one of the following effects:
  (a) A transient wind field exists even far away from the structure (e.g., change in wind direction or in strength, sudden gust of wind).
  (b) Owing to the shape of the structure, the flow becomes time dependent in the wake of the building (e.g., generation of a von Kármán vortex street past bluff bodies impigned by a constant wind).
  (c) Combination of (a) and (b).

Concerning the early fluid–structure coupling approaches and the practice in building dimensioning, in most cases only one of the disciplines is treated with a more complex model, whereas the other uses a simplified approach. This observation can be attributed to the circumstance that typically either fluid dynamics or structural mechanics specialists carried out these investigations, putting special emphasis on their specific field of knowledge and strongly simplifying the rest.

One possibility for a simplified structural model is to suppose the structure to be a rigid body with linear or torsional springs as bearing, while the flow field is described in more detail. Different levels of approximations have been used for this purpose, starting with computations based on the *potential theory* for isentropic and nonrotational flow. The next level is given by the *Euler equations* for inviscid fluid flows. Finally, with increasing computer power, the full *Navier–Stokes equations* have been solved for viscous flows. As an example of strong simplification on the structural side, the common section models of suspension bridges should be mentioned here (see, e.g., Frandsen, 1999).

In contrast, there are dynamic simulations of structures with a huge number of degrees of freedom, but the wind loads are modelled by statistical and half-empirical approaches (e.g., Kovacs, 1994; Zahlten, 1998) or even roughly estimated in the hope of meeting the worst load case.

Over the last few years, interdisciplinary formulations have been published involving both *improved flow models* and *flexible structures*. Furthermore, many groups have carried out research developing the coupling methodology. They provided or verified a variety of worthwhile algorithms including the simple sequential staggered coupling approach and parallel techniques including predictor–corrector steps, fluid subcycling, and adaptive under-relaxation. Examples are to be found in Bathe et al. (1995), Lesoinne and Farhat (1998), Le Tallec and Mouro (1998), Steindorf and Matthies (1999), and Wall et al. (1999).

Some examples concerning case (1) in the survey above have recently been investigated by Glück et al. (2001); others can be found in Section 4.2. For higher Reynolds numbers, the same configuration leads to case (2b); Section 5 presents an example of case (2a).

For this purpose the CFD code *FASTEST-3D* (Durst and Schäfer, 1996) developed by the Institute of Fluid Mechanics, Erlangen (Germany), and the CSD code *ASE* (Katz and Bellmann, 1995a) provided by SOFiSTiK AG, Munich (Germany), have been adapted and coupled by the *MpCCI* interface (Ahrem et al., 2000).

The paper is organized as follows: Section 2 provides the *governing equations* for the fluid flow and the structural dynamics including the boundary conditions. In Section 3 the *numerical methodologies* for both parts are described. Special emphasis is also placed on the coupling approach. The *application* of the method to an academic test case is analyzed and discussed in Section 4. Finally, the application to a coupled problem from civil engineering is investigated in Section 5.

2. Governing equations and boundary conditions

2.1. Fluid dynamics

Viscous fluid flow is governed by the *Navier–Stokes equations* expressing the conservation of *mass* (Eq. (1)) and *momentum* (Eq. (2)). For an incompressible fluid with constant properties as assumed in this study, the transport

equations read as follows:

$$\frac{\partial U_i}{\partial x_i} = 0, \tag{1}$$

$$\rho\left(\frac{\partial U_j}{\partial t} + U_i \frac{\partial U_j}{\partial x_i}\right) = -\frac{\partial P}{\partial x_j} + \mu \frac{\partial^2 U_j}{\partial x_i \partial x_i}, \tag{2}$$

where U_j is the velocity component in the j direction, x_i the cartesian coordinate in the i direction, P the pressure, ρ the density, and μ the dynamic viscosity of the fluid.

For the *boundary conditions* of a fluid domain the following distinction is drawn.

(i) *Inlet*: Velocity profiles $U_j(x_i)$ are usually given for the inflow.

(ii) *Outlet*: As the values of the flow variables are not a priori known at an outlet, a zero gradient for the velocity components is presumed normal to the outflow:

$$\frac{\partial U_j}{\partial x_i} n_i = 0, \tag{3}$$

which is a sufficient approximation if the outflow boundary is far enough from the main region of interest.

(iii) *Wall*: The no-slip boundary condition is valid at walls. For *resting walls* the flow velocity is zero at the wall:

$$U_j = 0, \tag{4}$$

and for *moving walls* the fluid adopts the wall velocity:

$$U_j = U_{\mathrm{w},j}. \tag{5}$$

(iv) *Symmetry*: If the flow problem is symmetric, the fluid domain for the calculations can be reduced, whereas the definition states that no fluid flows through symmetry boundary planes. Hence the velocity component normal to this plane is zero:

$$U_i n_i = 0. \tag{6}$$

2.2. Structural dynamics

The characteristics of *thin-walled structures* such as shells or membranes can be described by *reduced models* specifying state variables acting in the middle plane of the structure. Starting from equilibrium conditions, the constitutive relations and the material equations for the dynamic nonlinear response of the structure can be summarized by the *equations of motion*:

$$\mathbf{M}\ddot{\mathbf{u}}(t) + \mathbf{C}\dot{\mathbf{u}}(t) + \mathbf{K}(\mathbf{u}(t))\mathbf{u}(t) = \mathbf{F}(t), \tag{7}$$

where $\mathbf{M}$ is the mass matrix, $\mathbf{C}$ the damping matrix representing the inner or structural damping, and $\mathbf{K}(\mathbf{u}(t))$ the stiffness matrix depending on the displacements $\mathbf{u}(t)$ in a nonlinear way. $\mathbf{F}(t)$ characterizes the load acting on the structure caused by the fluid (pressure and shear stress). $\dot{\mathbf{u}}(t)$ and $\ddot{\mathbf{u}}(t)$ describe the velocity and the acceleration. It should be noted that any fluid damping is included on the right-hand side of Eq. (7) and *not* in the damping matrix $\mathbf{C}$.

Boundary conditions are defined on each part of the boundary and consist of two types.

(i) *Displacement boundary conditions*:

$$\mathbf{u} = \bar{\mathbf{u}}. \tag{8}$$

(ii) *Traction boundary conditions*:

$$\mathbf{T} = \bar{\mathbf{T}}, \tag{9}$$

where $\bar{\mathbf{u}}$ and $\bar{\mathbf{T}}$ are specified quantities for the displacement and the traction. Additionally, *initial conditions* have to be defined for the position and the velocity of the structure at some initial time t_0.

3. Numerical approaches

3.1. Fluid dynamics

For the solution of the Navier–Stokes equations based on a *finite volume* approach as used in the present work, it is advantageous to write the governing equations in integral form. For moving grids the integration of Eqs. (1) and (2) is

Table 1
Terms of the general transport Eq. (10)

Equation	Φ	Γ_Φ	s_Φ
Mass conservation	1	0	0
Momentum conservation	U_j	μ	$-\frac{\partial P}{\partial x_j}$

carried out for a control volume (CV) whose boundaries move with time. Applying the *Leibniz rule* and *Gauss theorem*, the general transport equation of the quantity Φ in a finite volume notation reads as follows:

$$\frac{\mathrm{d}}{\mathrm{d}t}\int_V \rho\Phi\,\mathrm{d}V + \int_S \left[\rho(U_i - U_{\mathrm{g},i})\Phi - \Gamma_\Phi \frac{\partial \Phi}{\partial x_i}\right]\mathrm{d}S_i = \int_V s_\Phi\,\mathrm{d}V. \tag{10}$$

For an incompressible fluid with constant properties, this equation is solved for both the continuity equation and the momentum equations; the corresponding values for the diffusion coefficient Γ_Φ and the source term s_Φ can be found in Table 1.

In the case of time-dependent moving meshes, the transport velocity is composed of the *Eulerian* or *absolute fluid velocity* U_i reduced by the *grid velocity* $U_{\mathrm{g},i}$. To ensure the conservation principle, the *space conservation law* (*SCL*) has to be fulfilled for each control volume (CV):

$$\frac{\mathrm{d}}{\mathrm{d}t}\int_V \mathrm{d}V - \int_S U_{\mathrm{g},i}\,\mathrm{d}S_i = 0. \tag{11}$$

According to Demirdžić and Perić (1990), the direct calculation of the grid velocities can be avoided by replacing them with the mass fluxes through the CV faces ('mesh fluxes') which result from the motion of the CV faces during the time step. The convective term in Eq. (10) containing the grid velocity can be discretized for a hexahedral CV as follows:

$$\int_S \rho\Phi\, U_{\mathrm{g},i}\,\mathrm{d}S_i \approx \sum_c \rho_c \Phi_c \frac{\delta V_c}{\Delta t}, c = \{\mathrm{w},\mathrm{e},\mathrm{s},\mathrm{n},\mathrm{b},\mathrm{t}\}, \tag{12}$$

where c stands for the six faces of the CV.

This means that the solution of each transport equation is based on the relative fluxes, which are the differences between the fluxes through a CV face caused by fluid motion reduced by the 'mesh fluxes'. Based on this formulation, the grid velocities $U_{\mathrm{g},i}$ are no longer required for the internal flow region but they have to be known explicitly at moving impermeable walls. This approach is the so-called *'arbitrary Lagrangian Eulerian* (*ALE*)' formulation (Demirdžić and Perić, 1990). Furthermore, the time-dependent term on the left-hand side of Eq. (10) has to be treated in a special way according to first- or second-order accuracy in the case of moving grids. Especially it has to be taken into account that not only the transported quantity Φ but also the cell volume ΔV is time dependent.

As mentioned above the CFD calculations were performed with *FASTEST-3D*. This is an incompressible, unsteady, three-dimensional finite volume code. The code is based on nonstaggered, block-structured grids and has been adapted to moving meshes. The terms for changing cell volumes, flux corrections, and wall velocities are discretized by a fully implicit scheme of second-order accuracy in time, consistent with the other time-dependent terms.

Concerning the spatial discretization, an upwind scheme (UDS) or a central-difference scheme (CDS) can optionally be used or combined based on a deferred correction approach. In the present study CDS was applied for all calculations in Section 4. For the complex geometry of the practical example in Section 5, only UDS provided converged solutions.

The *ALE* extension of *FASTEST-3D* was verified at several test cases. One example concerns the flow in a channel with a moving obstacle, which was investigated experimentally by Pedley and Stephanoff (1985) and calculated by Ralph and Pedley (1988), Demirdžić and Perić (1990), and others. The results coincide very well with the measurements and the other numerically predicted data.

3.2. Structural dynamics

The solution of the structural problem is based on the *finite element* method. The structure is discretized by a mesh of quadrilateral elements. With respect to the mechanical model, dimensionally reduced element formulations for membranes or shells are used based on a classical isoparametric formulation or a nonconforming formulation (see, e.g., Bathe, 1982; Zienkiewicz and Taylor, 1991). As mentioned before, the structural simulations were performed using the commercial program *ASE*, which incorporates special extensions adapted to the requirements in civil engineering (Katz and Bellmann, 1995a).

The time-dependent problem is solved by applying a *Newmark–Wilson* approach (Katz and Bellmann, 1995b). Assuming a linear acceleration within a time step, this implicit scheme is unconditionally stable and second-order accurate in time for linear and first-order accurate for geometrically nonlinear problems (Zienkiewicz and Taylor, 1991).

In addition to geometrical nonlinear effects such as large displacements in connection with small deformations, nonlinear material properties can be taken into account. For solving the system of nonlinear equations a modified Newton–Raphson scheme is used within each time step of the dynamic simulation.

3.3. Fluid–structure coupling

3.3.1. Geometric modeling and grid definition

In the design process for civil engineering constructions, the *geometric model* of the structure plays an important role. Therefore, it is also the central point in the software system architecture shown in Fig. 1. All geometric information is derived directly from given CAD data and stored in a database describing a *b-rep* (boundary representation) model (Bungartz et al., 1996; Corney, 1997) completed by information concerning material properties and boundary conditions.

For *membrane* structures it is also possible to start from an initial geometry and to determine the surface geometry under dead load in a so-called *'form finding process'* according to Bellmann (1998).

In a next step the surface of the structure is discretized by an *unstructured quadrilateral mesh* (see, e.g., Fig. 2) generated by an automatic mesh generator (Rank et al., 2000). The input data for the CFD grid generator *ICEM-CFD*, used to create a three-dimensional *block-structured hexahedral grid*, is also derived directly from the geometric model. Fig. 2 shows an example of the corresponding CFD surface grid of the tent roof, described in detail in Section 5. The CFD code treats the structure as an infinitely thin obstacle, whereas the real thickness is taken into account for the structural simulation.

3.3.2. Coupling algorithm

Both the CSD code *ASE* and the CFD code *FASTEST-3D* are highly adapted to their specific field of application, providing many special features. To preserve these advantages and to realize an effective coupling algorithm, a *partitioned* solution approach was chosen. Similar partitioned algorithms were used by other authors, e.g. Bungartz et al. (1998), Cebral (1996), Steindorf and Matthies (1999), and Wall et al. (2000). The simulation is based on an iterative frame algorithm, integrating both codes developed completely independently from each other in an *implicit* time-stepping procedure (see Figs. 1 and 3).

Each simulation code runs on its own processor(s) after being generated by a main process. The interprocess communication is supported by the *MPI Library* (MPI, 2001). Caused by the large difference in the number of grid

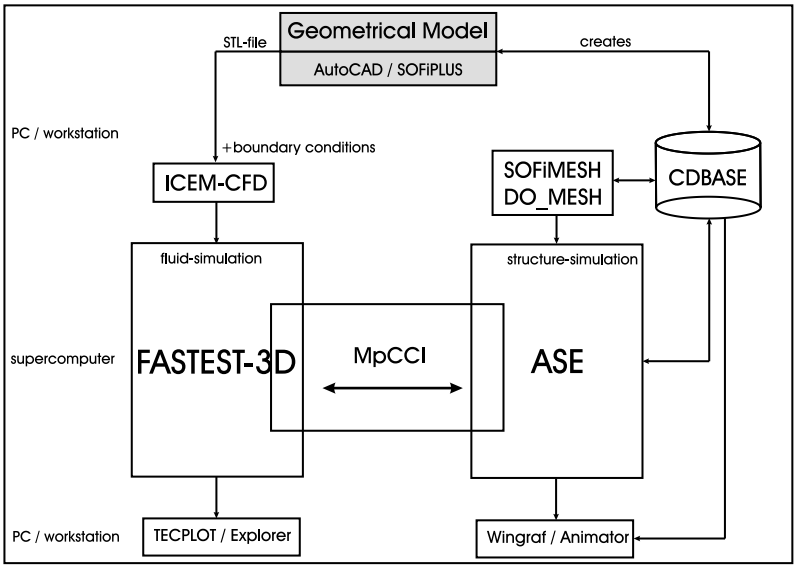

Fig. 1. Scheme of the software system architecture for the fluid–structure coupling.

points (e.g. 10^6 control volumes for CFD and 10^3 finite elements for CSD), the computational effort for the CFD part is much higher than that for the CSD part. However, the high vectorization and parallelization rate of *FASTEST-3D* allows efficient computations on parallel or vector-parallel machines and the use of multiple processors based on the domain decomposition approach.

All computations were carried out on the symmetric multi-processing (SMP) cluster *Hitachi SR8000-F1* at LRZ in Munich (Germany) applying up to seven of a total of 112 nodes. Each node consists of eight superscalar RISC processors (1.5 GFlops peak performance) having pseudo-vector properties. These improve the memory bandwidth, alleviating the main deficit of RISC-based high-performance computing (Brehm et al., 2001). The architecture of the *HITACHI SR8000-F1* allows the use of three different levels of parallelization: (i) *pseudo-vector processing*, (ii) *intra-node auto-parallelization* over all processors of one SMP node (via *COMPAS*), (iii) *inter-node parallelization* using several SMP nodes and a communication library for the data exchange between the nodes such as MPI. All three levels are taken into account to achieve a high performance of the CFD code.

The bilateral data exchange between CSD and CFD is managed using the *MpCCI coupling interface* (Ahrem et al., 2000). The exchange of element- and node-based variables between two nonmatching grids (FE vs. FV) is supported by a *neutral geometric model*. Although both grids approximate the same surface, their nodes do not coincide. Therefore, some mutual interpolation is necessary.

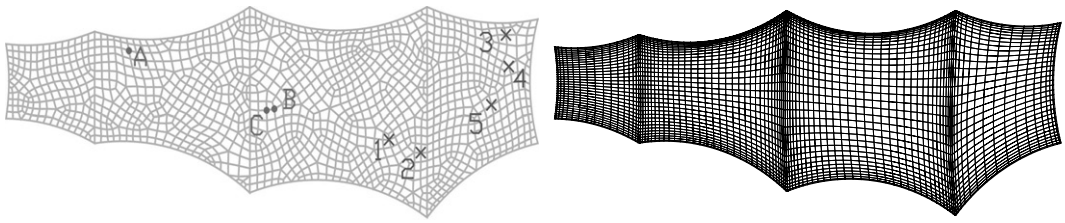

Fig. 2. CSD mesh of the tent roof with evaluation points (left) and CFD mesh layer adjacent to the tent roof (right). Both are projected into the x–y plane.

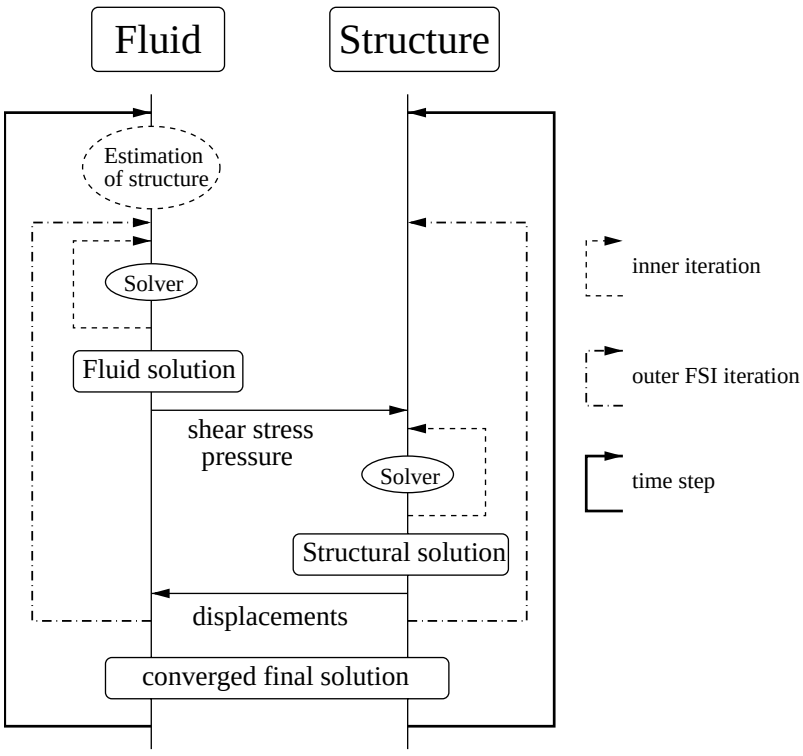

Fig. 3. Detailed overview of the partitioned coupling algorithm.

For the transfer of *pressure forces* and *shear forces* from CFD to CSD, a *conservative interpolation* according to Farhat et al. (1998) is used, ensuring that the load resultants on both grids are exactly the same. The disadvantage of this method is that in case of a coarse source grid and very fine target grid, the loads are distributed in a nonphysical way. However, usually the CFD mesh is finer than the CSD grid anyway.

The calculated *displacement vectors* of the CSD nodes are transferred to the CFD nodes by using a *bilinear interpolation* in order to be consistent with the bilinear ansatz functions used for the finite element calculation of the structural displacements in the CSD code. A conservative interpolation as used to transfer pressure forces and shear forces is not suitable here, because the displacements are not integral quantities.

The coupling algorithm controlling the time-stepping procedure in the iterative solution process based on Dütsch et al. (1999) is shown in Fig. 3. The outer loop describes the temporal discretization of the problem. Within each time step, outer iterations between the CFD and CSD simulation are performed until *global convergence* is reached, i.e. the coupling scheme is *fully implicit*. Thereby, the threshold for the residual structural displacements is usually 10^{-4}–10^{-3} times the maximum amplitude of oscillation in the case of dynamic fluid–structure interactions. The load for the CSD simulation is computed from the *pressure* and *shear stresses* as a result of the CFD computation and the boundary geometry is modified by the *structural displacements* computed by the CSD simulation. Significant structural deformations can be taken into account by an under-relaxation of the boundary geometry. To reduce the number of outer iterations within each time step of the dynamic coupling procedure, this strategy is extended by a *predictor–corrector scheme*. At the beginning of each time step, the boundary geometry is estimated from the results of previous time steps, and the geometries of the last three time steps are taken into account in order to estimate the geometry for the new time step with second-order accuracy in time. Based on this geometry, a CFD simulation is carried out followed by a CSD computation which corrects the predicted interface geometry used in the next fluid–structure interaction (FSI) iteration as shown in Fig. 3. Using the above-mentioned geometry estimation, the number of CFD iterations could be reduced by up to 45% (Glück et al., 2001).

3.3.3. *Adaptation of the CFD grid*

During each outer fluid–structure iteration, the finite volume grid of the fluid domain has to be adapted to the new position of the boundaries. This is done in special routines using *algebraic methods* (linear distortion in the inner region of a grid block as standard method, transfinite interpolation or use of special problem-adapted higher-order polynomials to generate the block faces in the vicinity of the distorted structure).

An example of a distorted mesh around a flexible vertical plate applying the last-mentioned method is given in Fig. 4. A transfinite interpolation (Thompson et al., 1985) was used for the test case in Section 4 in order create the block face including the distorted edges $\overline{DE}$ and $\overline{EF}$ depicted in Fig. 5.

4. Application to test case: L-shaped plates

The first test case is an academic one in order to study phenomena such as vortex shedding in the three-dimensional wake behind an oscillating bluff body, resonance concerning the vortex-shedding frequency and an eigenfrequency of the structure, and the interaction between several flexible plates caused by the surrounding fluid.

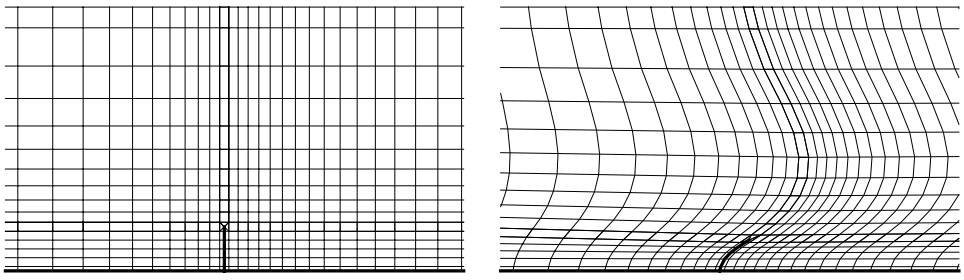

Fig. 4. 2D-cut through a 3D initial mesh (left) and distorted mesh (right) around a flexible vertical plate using a polynomial of third order to generate the block interface upwardly adjacent to the plate and linear distortion of the inner grid points inside the blocks.

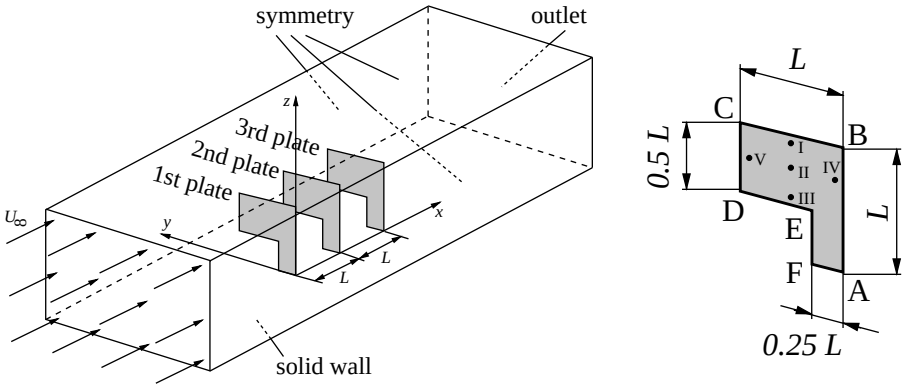

Fig. 5. Arrangement of the L-shaped plates test case and positions of chosen points on the plate for pressure analysis.

Table 2
Simulated test cases concerning L-shaped plates

No. of L-plates	Re	U_∞ (m/s)	$E/(\frac{1}{2}\rho U_\infty^2)$	Δt (s)	Wake pattern	Remark
1	50	10	7.00×10^7	0.025	Stationary	
1		10	7.00×10^7	0.025	Periodic	
1	200	5.48	23.31×10^7	0.025	$\Rightarrow$ 2 individual frequencies	$f_1 = f_{e,1} = 1.19$ Hz
1		14.07	3.54×10^7	0.01		$f_1 = f_{e,2} = 3.15$ Hz
1		10	7.00×10^7	0.025	Quasi-periodic	
2		10	7.00×10^7	0.025	$\Rightarrow$ Wider range of frequencies	
3	500	10	7.00×10^7	0.025		
3		16	2.73×10^7	0.025		

4.1. Description of the configuration

Fig. 5 illustrates the arrangement of several flexible, L-shaped plates, each of them clamped at their shortest edge $\overline{FA}$. The extensions of the flow domain were $L_x = 40$ m, $L_y = 11$ m, and $L_z = 6$ m. Three laminar flow configurations defined by the Reynolds number referred to the length L and the relevant free-stream velocity U_∞ were taken into account (see Table 2), each of them representing one characteristic regime: *laminar steady wake* (Re = 50), *unsteady periodic wake* (Re = 200), and *aperiodic wake* (Re = 500). All simulations were carried out without any turbulence model, because even for the highest of these Reynolds numbers transition will not occur in the near vicinity of the plates, but only in the remote wake.

For Re = 200 the far-field velocity was varied, leading to completely different structural responses, because it is not only the Reynolds number that is a characteristic parameter to describe the coupled problem. As a measure of the resistance of the structure against the fluid load, the *ratio* of the *modulus of elasticity* E and the *stagnation pressure* ($\rho U_\infty^2/2$) is also given in Table 2. For Re = 500 the mutual influence of several plates was examined.

Until a time of $t = 20$ s after the beginning of the FSI simulation, the plates were *fixed* and *rigid*, i.e., only the flow was calculated. After that moment the plates became *flexible*, so that they were able to oscillate freely in the flow. Only the clamp support at $\overline{FA}$ was still maintained. The free-stream velocity U_∞ was constant during each of these simulations. The geometric data and structural properties of one L-plate are given in Table 3.

The time-step size for the coupled simulations was $\Delta t = 0.025$ s in order to resolve one oscillation period with the first eigenfrequency of the plate by at least 30 time steps, which was found to be sufficient. The only exception is the test case with Re = 200 and $U_\infty = 14.07$ m/s, where a time-step size $\Delta t = 0.01$ s was used in order to resolve the oscillations with the second eigenfrequency.

Figs. 6 and 7 show the CFD surface grids used and also the different CSD grids, whereas all simulations described in Table 2 are based on the finest mesh *CFD 3* in connection with the structured mesh *CSD 1*. Detailed information

Table 3
Characteristics of one L-shaped plate

Length	$L = 1$ m
Thickness	$d = 10$ mm
Material	Polyester
Modulus of elasticity	$E = 3500$ MN/m^2
Shear modulus	$G = 1326$ MN/m^2
Poisson's ratio	$v = 0.32$
Density	$\rho = 1200$ kg/m^3
Eigenfrequencies[a]	$f_{e,1} = 1.19$ Hz $f_{e,2} = 3.15$ Hz $f_{e,3} = 10.11$ Hz $f_{e,4} = 18.78$ Hz …

[a] Calculated with the CSD code *ASE* using *Lanczos*' method (Bathe, 1982).

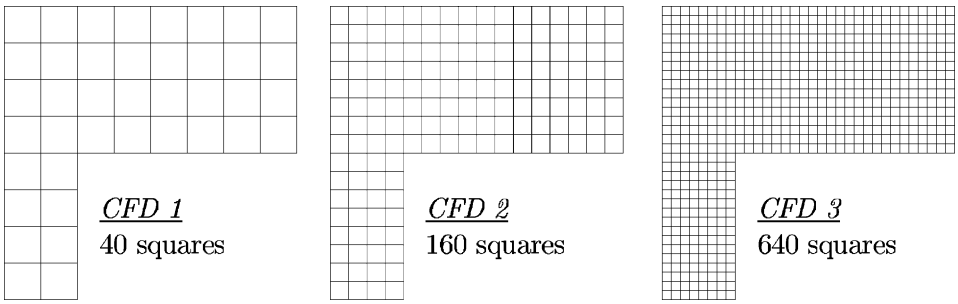

Fig. 6. CFD surface grids for the L-shaped plates.

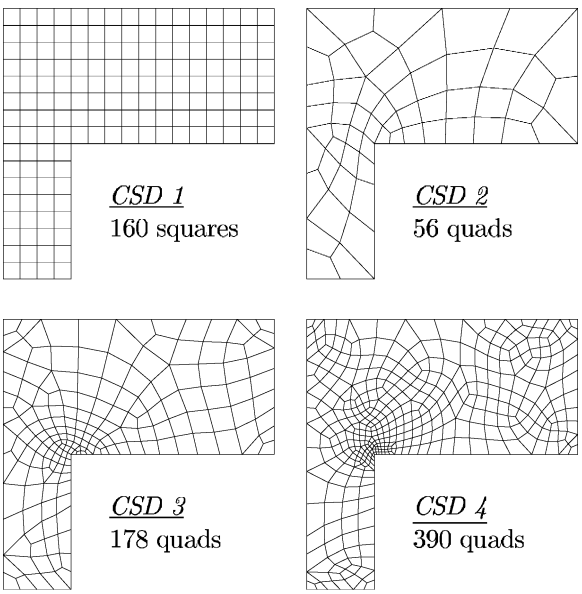

Fig. 7. CSD grids for the L-shaped plates.

Table 4
Data on the CFD grids for the L-shaped plate problem

No. of plates	Grid	No. of blocks	No. of control volumes (CV)		
			In x, y, z direction	Total	On the plate
1	*CFD 1*	24	$36 \times 24 \times 16$	13,824	40
1	*CFD 2*	24	$72 \times 48 \times 32$	110,592	160
1	*CFD 3*	24	$144 \times 96 \times 64$	884,736	640
2	*CFD 3*	36	$168 \times 96 \times 64$	1,032,192	640
3	*CFD 3*	48	$184 \times 96 \times 64$	1,130,496	640

concerning the CFD volume grids is given in Table 4. All CFD grids are nonequidistant, and have a higher resolution near the bottom wall and the L-plates. The influence of the grid resolutions of the CFD and the CSD domain will be discussed separately in Section 4.2.1.

Furthermore, the behavior of the (implicit) coupling algorithm *with* FSI iterations within each time step (see Section 3.3.2) was studied in comparison with an (explicit) frame algorithm *without* any FSI iterations. For the latter, two different time-step sizes were used.

The coupled simulations were carried out on seven nodes of the *Hitachi SR8000-F1* (six nodes for CFD, one node for CSD).

4.2. Results

4.2.1. *Laminar steady flow* (Re = 50)

Fig. 8 represents the displacement of the outer vertex C of the plate over time. As mentioned in Section 4.1, the plate had been fixed until $t = 20$ s. Thereafter the constraint was released and the plate was able to perform structural oscillations. Because of the sudden release of the plate, the displacement overshot several times the *steady deformation state*, which had been reached after a few seconds. A Fourier transformation of the displacements clarified that the plate oscillates mainly in its first eigenfrequency of $f_{e,1} = 1.19$ Hz.

The reason for the standstill of the plate after a while is the *stationary flow field* around the plate which coincides with the small Reynolds number chosen. The pressure curve for a point at the back side of the plate in Fig. 9 only shows pressure oscillations due to the movement of the plate. More details (e.g., a vertical and a horizontal cutting plane through the pressure field) can be found in Binder (2001).

Influence of the CFD grid resolution: The three grid levels *CFD 1*, *CFD 2*, and *CFD 3* in Fig. 6 were applied to the calculation of the (steady) flow field around the fixed and rigid plate ($t < 20$ s) in order to study the CFD grid dependence. Table 5 shows the results for the pressure difference between the front and back sides of the L-plate at point II in Fig. 5. The *Richardson extrapolation* (Ferziger and Perić, 1999) based on the grid levels *CFD 2* and *CFD 3* and on the theoretical order of the used central difference scheme (CDS) $p = 2$ yields the *grid independent solution* in Table 5. The deviation on grid level *CFD 3* of only 0.27% is highly satisfactory for practical simulations.

Influence of the CSD grid resolution: Fig. 10 represents the displacements of the vertex D for the four different CSD meshes depicted in Fig. 7 predicted with the finest *CFD 3* grid in Fig. 6. Vertex D was chosen, because at this location the coarsest *CSD 2* mesh with 56 elements yielded the largest deviation from the structured *CSD 1* mesh with 160 elements. However, the deviation of the coarsest mesh is not larger than 2.6%, so that even this mesh provides satisfactory results for practical purposes.

Explicit vs implicit frame algorithm and influence of the time-step size: As mentioned in Section 3.3.2. a *fully implicit predictor–corrector scheme* was used for all simulations in the present work. The only exceptions are to be found in this subsection, where the fully implicit scheme was compared with an *explicit scheme* without any subiterations within each time step. This means that the outer FSI iterations in Fig. 3 were omitted. Furthermore, the difference between the explicit schemes with and without a *predictor step* (estimation of the structure in Fig. 3) were investigated, and three different time-step sizes were taken into account for each of these two explicit schemes.

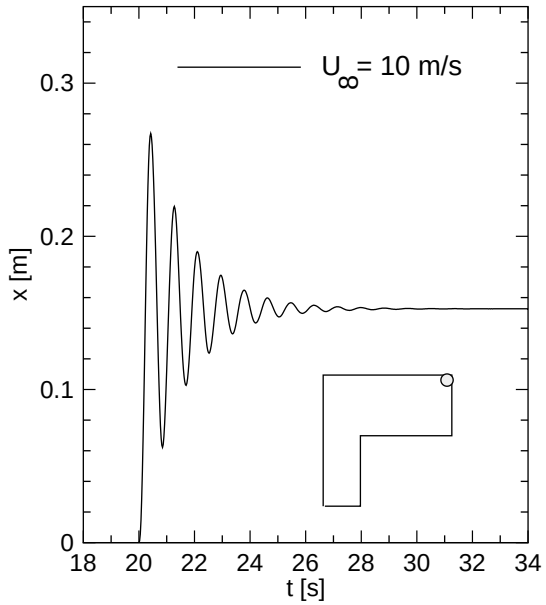

Fig. 8. Time history of the displacement of vertex C at Re = 50.

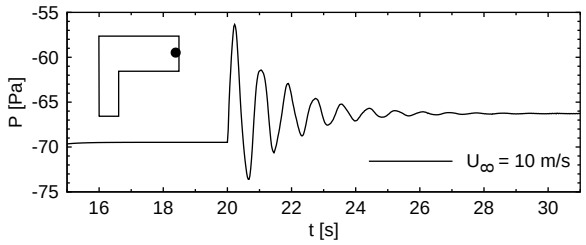

Fig. 9. Time history of the pressure at point V on the back side of the plate at Re = 50. (In all figures showing pressure signals the pressure is given *relative* to the reference pressure at the inlet to the flow field leading to partially negative values.)

Table 5
Pressure difference between the front and back sides of the L-shaped plate at point II in Fig. 5 for Re = 50 obtained on different grid levels (grid independent solution estimated by *Richardson extrapolation*)

Grid level	ΔP_{II} (Pa)	Deviation from grid independent solution (%)
CFD 1	53.73	−3.15
CFD 2	54.87	−1.10
CFD 3	55.33	−0.27
Grid independent solution	55.48	—

The results of the mentioned simulations are depicted in Figs. 11–16. The output of the implicit-coupled calculations with a small time-step of $\Delta t = 0.025$ s (see Fig. 8) is given as *reference solution*.

Concerning the explicit scheme *without* prediction of the structural shape at the beginning of a new time step, the following resulted: the amplitudes of the damped oscillations were much too high for all time-step sizes, but this phenomenon extenuated slightly with decreasing time-step size, which is typical for an explicit scheme. On the other hand, *instabilities* in the displacement curve occured the earlier, the smaller was the time-step size (see Figs. 11–13). This

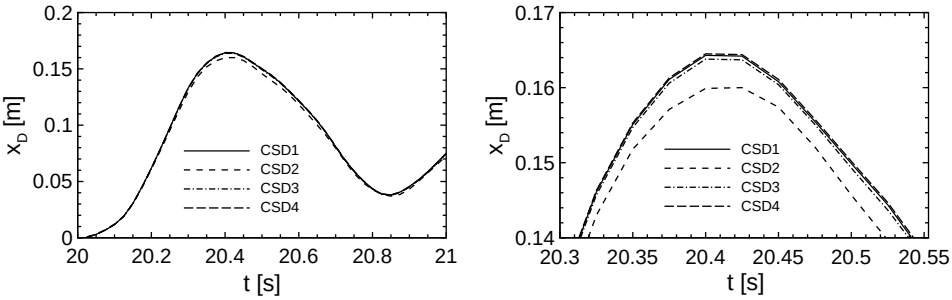

Fig. 10. Comparison of the displacements at vertex D obtained by the different CSD meshes in Fig. 7 at Re = 50 (right: zoom of left diagram).

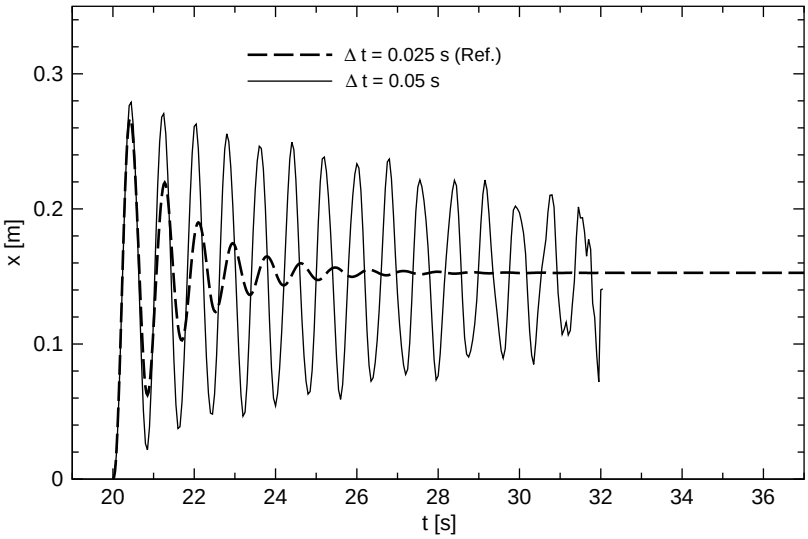

Fig. 11. Time history of the displacement of vertex C at Re = 50 (explicit scheme *without* predictor step with $\Delta t = 0.05$ s in comparison with the implicit reference solution).

observation agrees with the results of Wall (1999), who described the increasing danger of instability with decreasing time-step size for explicit coupling procedures.

In contrast to the explicit scheme without a predictor step, the explicit scheme *with* a predictor step is far more *accurate* within its stable period of time. For a time-step size which was small enough to resolve the structural oscillations ($\Delta t \leqslant 0.025$ s, see Figs. 15 and 16), the displacement curves can hardly be distinguished from the reference solution. On the other hand, the explicit scheme *without* a predictor step is *stable* for a much longer time span, even though producing large deviations from the reference solution. Mok and Wall (2001) investigated a similar numerical example. They found exactly the same conflicting phenomena as mentioned above. In their nomenclature the explicit scheme without a predictor step is denoted 'basic sequential staggered', the explicit scheme with a predictor step 'sequential staggered with predictor', and the implicit (reference) scheme as 'iterative staggered'. Mok and Wall (2001) drew the same conclusion as in the present study, that only the implicit coupling scheme is appropriate to produce stable and accurate solutions. Le Tallec and Mouro (1998) also pointed out that it is difficult to stabilize explicit coupling schemes.

Concerning the explicit scheme *with* a predictor step another issue should be mentioned: in contrast to the scheme without a predictor step the solution became unstable in both cases, for decreasing and increasing time-step size starting from $\Delta t = 0.025$ s, which can be seen in Figs. 14–17.

4.2.2. Unsteady periodic flow (Re = 200)

The influence of three different free-stream velocities on the structural response was investigated at the same Reynolds number Re = 200.

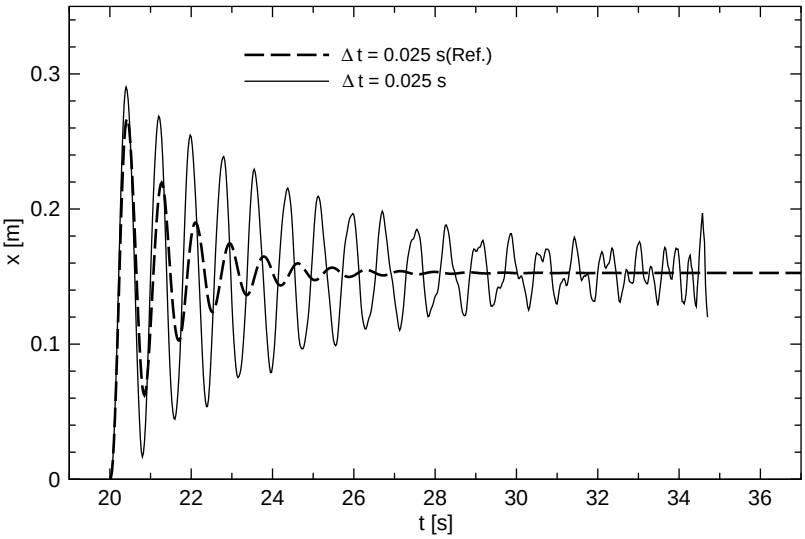

Fig. 12. Time history of the displacement of vertex C at $\mathrm{Re} = 50$ (explicit scheme *without* predictor step with $\Delta t = 0.025$ s in comparison with the implicit reference solution).

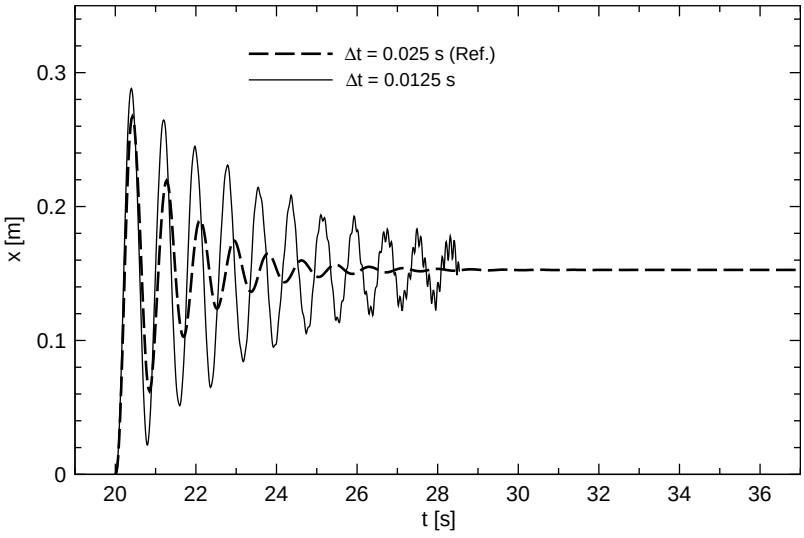

Fig. 13. Time history of the displacement of vertex C at $\mathrm{Re} = 50$ (explicit scheme *without* predictor step with $\Delta t = 0.0125$ s in comparison with the implicit reference solution).

Arbitrarily chosen free-stream velocity ($U_\infty = 10$ m/s): Corresponding to Section 4.2.1, first the arbitrarily chosen velocity $U_\infty = 10$ m/s was considered. Although the vortex shedding in the wake has a complex three-dimensional structure (see, e.g., Fig. 18), there are some phenomena which should be examined more closely. The pressure histories for the five points in Fig. 5 on the back side of the (still fixed and rigid) plate are shown in Fig. 19. The pressure values at points IV and V oscillate exactly in opposite phase, while the pressure at I lags only approximately $\pi/2$ behind the pressure at III.

A Fourier transformation yields two main frequencies in each signal, $f_1 = 2.15$ Hz and $f_2 = 4.3$ Hz, where the second one is exactly twice the first (see Figs. 21 and 22 and Table 6). The *Strouhal numbers* Sr_1 based on f_1 and the *width* L of the plate and Sr_2 based on f_2 and the *height* $0.5L$ of the flag-like part of the plate are $Sr_1 = Sr_2 = 0.215$, which is a typical value for vortex shedding behind bluff bodies. Both Strouhal numbers use U_∞ as characteristic velocity, which is legitimate, because for both $\mathrm{Re} = 200$ and 500 the flag-like part of the L-plate is situated outside of the boundary layer near the ground wall.

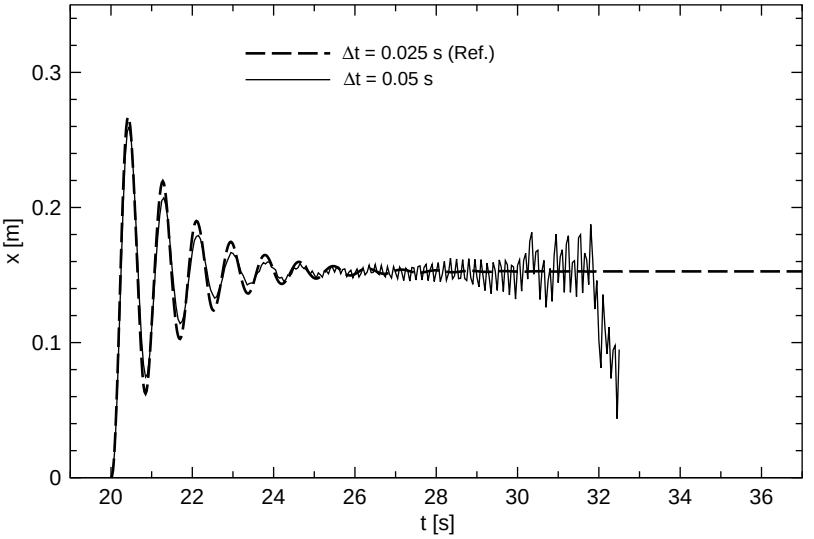

Fig. 14. Time history of the displacement of vertex C at Re = 50 (explicit scheme *with* predictor step with $\Delta t = 0.05$ s in comparison with the implicit reference solution).

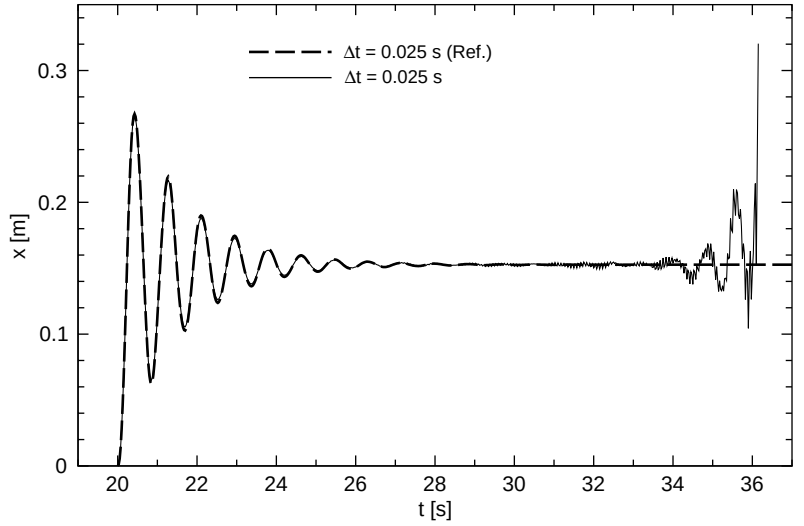

Fig. 15. Time history of the displacement of vertex C at Re = 50 (explicit scheme *with* predictor step with $\Delta t = 0.025$ s in comparison with the implicit reference solution).

After the plate became flexible at $t = 20$ s, the structural response is similar to the case with Re = 50. The plate reaches a steady deformation state after some initial oscillations (see Fig. 20). In the pressure distribution for $t \geqslant 20$ s, three dominant frequencies are found as given in Table 6. The first one, 1.19 Hz, is due to the movement of the plate in its first eigenfrequency. The further two are the vortex-shedding frequencies at the deformed plate. With respect to the frequencies observed for $t < 20$ s, both values are slightly shifted to larger values. This can be explained as follows: the *blocking* length scale of the flag-like part of the L-plate in the z direction is $L/2$ for the vertical resting plate at $t < 20$ s, but lower than $L/2$ for the distorted plate at $t > 20$ s. The Strouhal number also changed slightly, because of the distorted shape. Both phenomena together led to slightly shifted vortex-shedding frequencies.

Free-stream velocity adjusted to resonance at first eigenfrequency ($U_\infty = 5.48$ m/s): Here U_∞ was adjusted in such a way that the main vortex shedding frequency was equal to the *first* eigenfrequency of the L-shaped plate in order to reach the *resonance case* (see Figs. 21 and 23 and Table 6). Fig. 20 underlines that the plate never came to a standstill; rather, the plate was excited to bending and torsional oscillations again and again.

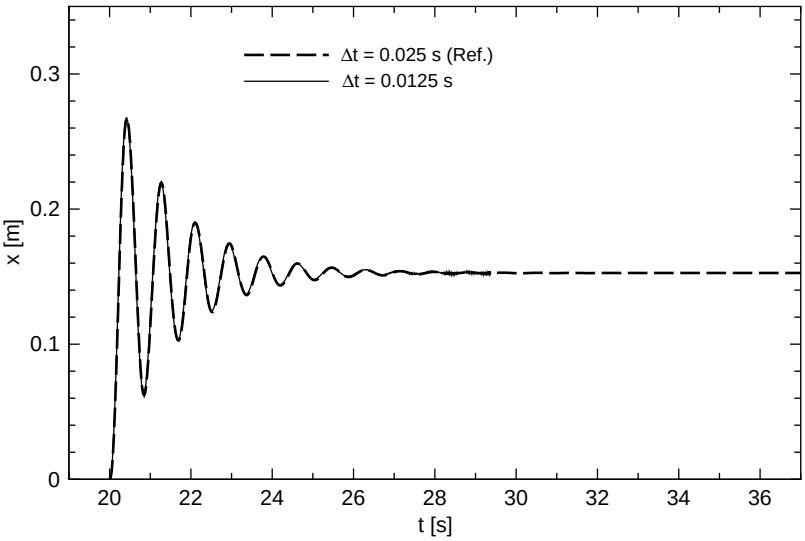

Fig. 16. Time history of the displacement of vertex C at Re = 50 (explicit scheme *with* predictor step with $\Delta t = 0.0125$ s in comparison with the implicit reference solution).

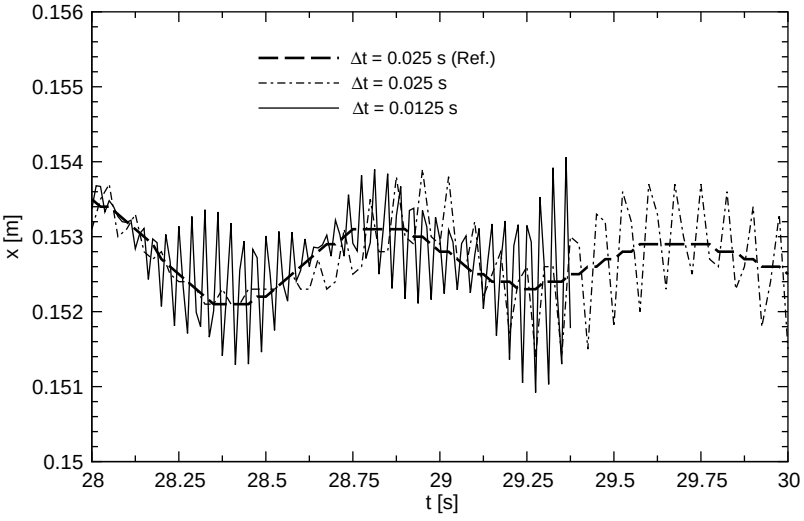

Fig. 17. Detail from Fig. 15 superimposed with Fig. 16.

Free-stream velocity adjusted to resonance at second eigenfrequency ($U_\infty = 14.07$ m/s): In this case U_∞ was adjusted such that the main vortex shedding frequency, 3.13 Hz, was nearly the same as the *second* eigenfrequency, 3.15 Hz, of the plate. Again a *resonance case* was found (see Figs. 21 and 24 and Table 6). For $t \geqslant 20$ s, besides the first and second eigenfrequencies, the two shifted vortex-shedding frequencies, 3.61 and 7.30 Hz, were found. In a zoomed version of Fig. 20, it can be seen that the plate also did not come to standstill, but oscillated in its second eigenfrequency, even though with a very low amplitude.

4.2.3. Aperiodic flow (Re = 500)

At Re = 500 the number of L-plates was varied in order to study the mutual influence to the structural response.

Single plate or two plates in a row: Corresponding to Sections 4.2.1 and 4.2.2, first the loading of the plate by $U_\infty = 10$ m/s was considered. The difference from the cases at the lower Reynolds numbers is that the plate did not reach a steady deformation state even for this arbitrarily chosen velocity of 10 m/s (see Fig. 25).

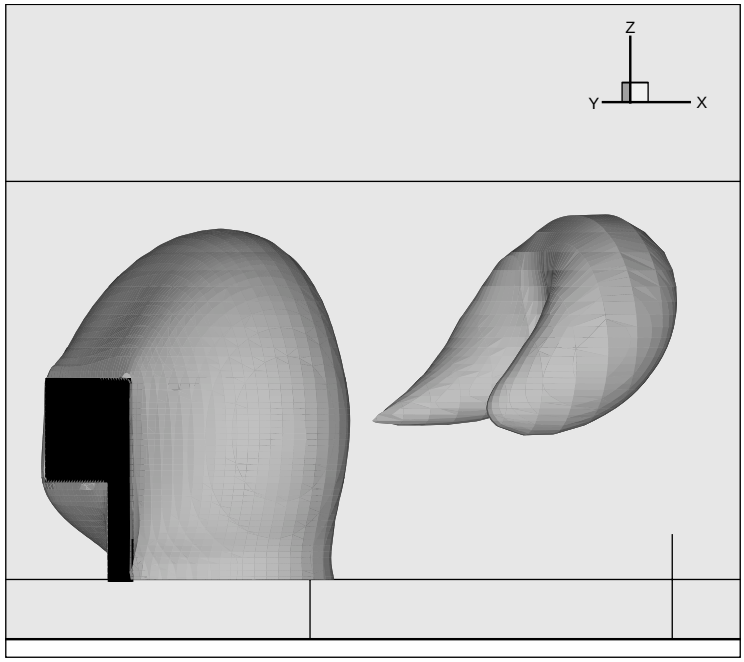

Fig. 18. Three-dimensional shedding and deformation of vortices past the L-shaped plate at Re = 200.

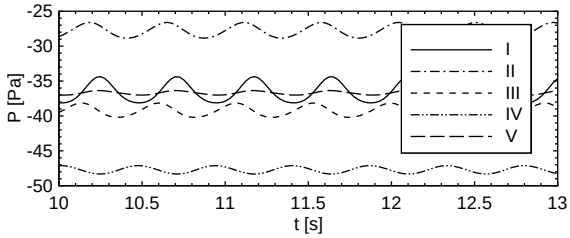

Fig. 19. Pressure at chosen points on the back side of the fixed and rigid plate ($t<20$ s) at Re = 200 and $U_\infty = 10$ m/s.

In the case of two plates, the first came to a standstill but the second did not (see Fig. 26), probably because the vortices from the rear plate can shed unhinderd, in contrast to the front plate. Both cases show an *aperiodic* wake structure.

Three plates in a row: In the case of three plates, the first came to standstill but the second and the third did not (see Fig. 27). The frequency spectra of the displacements are depicted in Fig. 28, showing that the first plate is oscillating nearly periodically in its first eigenfrequency, whereas the second and third were excited to perform oscillations also in their second eigenfrequency. The appearance of the second eigenmode is also found in the visualization of the structural behavior. Beyond this, the displacement signals of plates 2 and 3 show a wide range of smaller frequency peaks, i.e., these plates do *not* oscillate purely *periodically*. This qualitative difference in the behavior of the first plate in comparison with the other plates was found in all calculations at Re = 500 for the arrangements consisting of two or three plates.

Concerning three plates, a higher free-stream velocity of $U_\infty = 16$ m/s was also taken into account. This is the example with the largest deformations of all structures due to the high stagnation pressure loading of the plates (see Fig. 29).

Fig. 30 represents the time history of the pressure at point V (see Fig. 5) on each plate. It becomes obvious that, in contrast to Re = 200, a wider range of frequencies can be found in the pressure signal even for $t<20$ s representing an *aperiodic* wake structure. For simpler bluff bodies such as the circular cylinder flow, this phenomenon is observed first in the range $220 \leqslant \mathrm{Re} \leqslant 400$ and is directly related to transition to turbulence ocurring in the wake behind the body. As expected, the largest pressure difference between the front and back sides occurred at plate 1. In contrast to plate 1, the

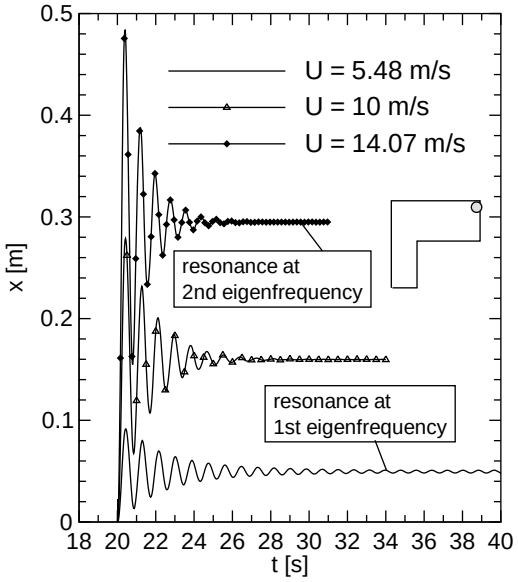

Fig. 20. Time history of the displacement of vertex C for different free-stream velocities U_∞ at Re = 200.

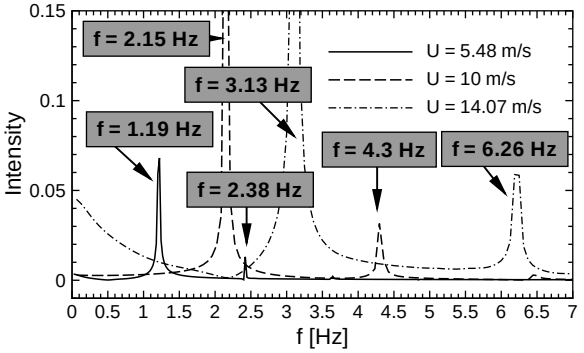

Fig. 21. Frequency spectrum of the pressure at point V on the back side of the plate for different free-stream velocities U_∞ at Re = 200 for $t < 20$ s.

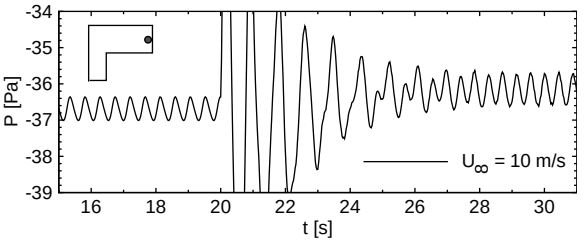

Fig. 22. Time history of the pressure at point V on the back side of the plate at Re = 200 and $U_\infty = 10$ m/s (arbitrarily chosen).

pressure on the front side of plate 2 is smaller than that on the back side at all times, leading to an average displacement of plate 2 in the opposite flow direction.

Fig. 31 depicts three snapshots of the pressure field in a vertical cutting plane through the flag-like parts of the three L-plates. The low-pressure area between the first two plates becomes obvious and the large distortion of plate 1

Table 6
Frequency peaks in the displacement of vertex C and in the pressure signal at point V on the back side of the plate before ($t<20$ s) and after ($t\geqslant 20$ s) the plate became flexible at Re = 200 (the intensities of the peaks each decrease with increasing frequency)

U_∞ (m/s)	Frequencies in displacement ($t\geqslant 20$ s) (Hz)		Frequencies in pressure ($t<20$ s) (Hz)		Frequencies in pressure ($t\geqslant 20$ s) (Hz)			
5.48	1.19		1.19	2.38	1.19	2.45		
10.00	1.19		2.15	4.30	1.19	2.29	4.65	
14.07	1.19	3.15	3.13	6.26	1.19	3.15	3.61	7.30

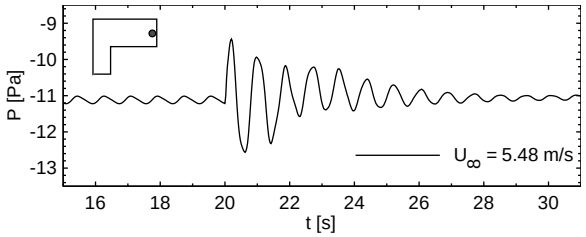

Fig. 23. Time history of the pressure at point V on the back side of the plate at Re = 200 and $U_\infty = 5.48$ m/s (adjusted to resonance at *first* eigenfrequency).

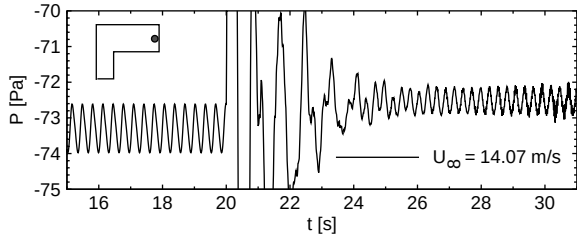

Fig. 24. Time history of the pressure at point V on the back side of the plate at Re = 200 and $U_\infty = 14.07$ m/s (adjusted to resonance at *second* eigenfrequency).

(top right), leading to a stronger exposure of plate 2 in the flow, which can be recognized in the pressure variation in Fig. 30 (middle).

5. Application to civil engineering: tent roof

The second test case deals with a real-life structure from the field of civil engineering in order to show that the coupling procedure is also able to handle more complex examples of practical interest.

5.1. Description of the configuration

The membrane roof in Fig. 32 was built in front of the entrance to an office building in Dresden (Germany) in 2000. This building acted in a slightly modified shape as a model for the present test case. Its technical data are given in Table 7. Between the pylons a thin glass-fiber membrane is tautened by circumferential cables.

The superposition of a *constant basic wind flow* and a *time-dependent wind gust* was taken into consideration to realize an unsteady fluid–structure interaction. In a previous investigation a constant wind flow did not lead to a dynamic response (Glück et al., 2001). In this first test case for a *dynamically* coupled calculation of the flow around a *membrane*

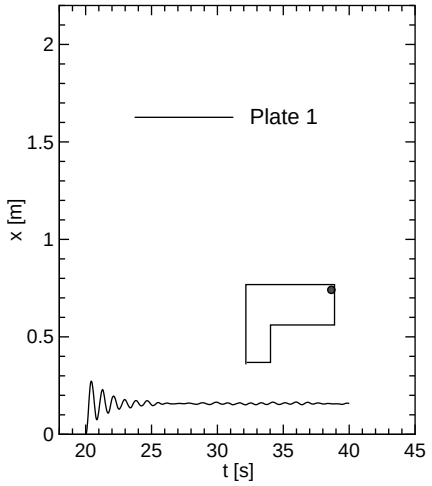

Fig. 25. Time history of the displacement of vertex C for one single plate at Re = 500 and $U_\infty = 10$ m/s.

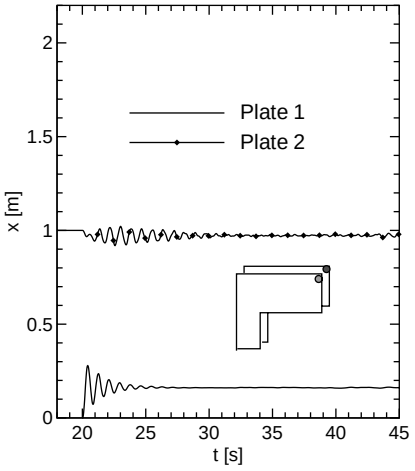

Fig. 26. Time history of the displacement of vertices C for two plates in a row behind each other at Re = 500 and $U_\infty = 10$ m/s.

structure, importance was attached first to the appropriate simulation of the structural response, whereas especially the structural oscillations at the end of the wind gust were to be examined.

For that reason and because of the known weakness of the k–ε model and related models based on the Reynolds-averaged Navier–Stokes equations for unsteady turbulent flows around bodies, a simulation of the turbulent wind field was not taken into account. This would require a large eddy simulation for the prediction of the turbulent flow (Breuer, 2002) which is the most reasonable and promising tool for an appropriate representation of the fluid flow for highly unsteady flow phenomena encountered in dynamically coupled simulations. For the purpose of this paper, however, a laminar flow was assumed with a Reynolds number of

$$\mathrm{Re} = \frac{L W_{\max}}{\nu} = 120 \tag{13}$$

formed with the leading edge of the roof ($L = 3$ m) and with the maximum gust velocity $W_{\max} = 40$ m/s.

The *basic flow* was assumed to be parallel to the ground in the positive x direction with $U_\infty = 10$ m/s at a height of 10 m above the ground. A *wind gust* was superimposed, which followed a Gaussian curve in both time

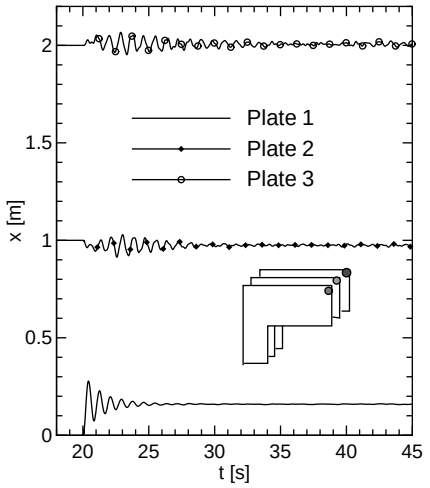

Fig. 27. Time history of the displacement of vertices C for three plates in a row behind each other at Re = 500 and $U_\infty = 10$ m/s.

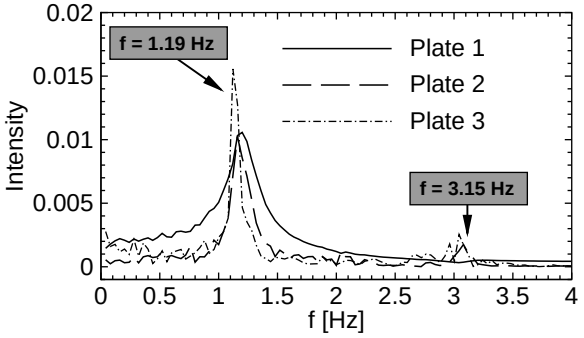

Fig. 28. Frequency spectrum of the displacement of vertices C for three plates in a row behind each other at Re = 500 and $U_\infty = 10$ m/s.

and space:

$$W(x,t) = W_{\max}\, \mathrm{e}^{-0.5(t-t_\mathrm{m})^2} \mathrm{e}^{-0.005(x-x_\mathrm{m})^2}, \tag{14}$$

with $x_\mathrm{m} = -12$ m and $t_\mathrm{m} = 3$ s. The vector of the inflow velocity is depicted in Fig. 33. It is given by

$$\mathbf{U}_{\mathrm{inflow}}(x,t) = \begin{pmatrix} U(z) \\ 0 \\ W(x,t) \end{pmatrix}. \tag{15}$$

Both the CFD and CSD simulations were based on a time step $\Delta t = 0.4$ s. The particular surface meshes have already been depicted in Fig. 2. The *CSD mesh* consists of 1409 nodes and 1311 finite elements, whereas the *CFD mesh* includes 1,024,000 finite volumes, of which 3072 contact the membrane surface. The flow domain had a length of $L_x = 144$ m, a width of $L_y = 33$ m, and a height of $L_z = 20$ m.

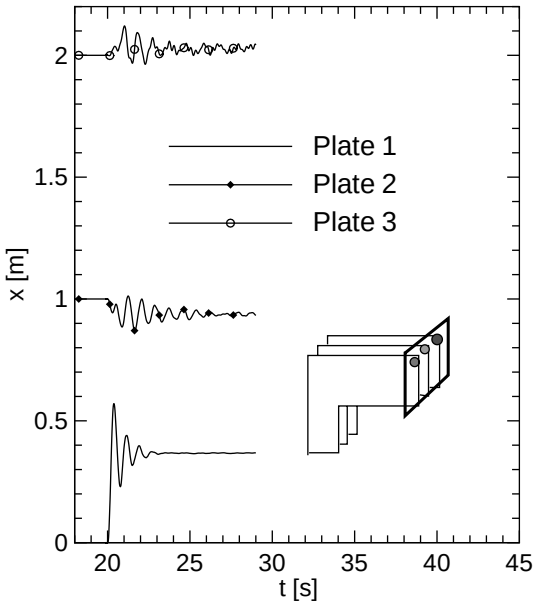

Fig. 29. Time history of the displacement of vertices C for three plates in a row behind each other at Re = 500 and $U_\infty = 16$ m/s.

5.2. Results

Fig. 34 shows a sample of four states of the flow field and the structural deformations at various time instants. The grey scales in the fluid represent the velocity magnitude near the walls, while the shading of the membrane embodies its deformation. A qualitative example for the output of the CSD code is given in Fig. 35 showing the fluid load and the displacement of the structure.

The largest displacement occurred at the maximum of the gust at $t = 3$ s, whereas the maximum distortion in the x direction is to be found at point A, in the y direction at point B, and in the z direction at point C, depicted in Fig. 36 (left). The locations of these characteristic points (A, B, C) are displayed in Fig. 2. The largest vertical displacement of about $\Delta z_{\max} = 0.3$ m (point C) is observed approximately in the middle of the tent.

Fig. 36 (right) shows the displacements in the z direction for the chosen evaluation points 1–5 also displayed in Fig. 2. It becomes obvious that some of the points were moving upwards and others downwards during the impact of the gust, which is more clearly visible in an animation of the coupled simulation available at http://www.lstm.uni–erlangen.de/ber3/index99_ber3.html. Points 1 and 2 showed a noticeable overshoot and subsequent small oscillations, before they reached the steady deformation state — which corresponds to the constant basic flow without superimposed wind gust — again.

An evaluation of the forces that occurred inside the material in both the x and y directions—which nearly coincide with the weft and warp directions of the fabric — yielded the *maximum membrane forces* $\sigma_x = 29.074$ kN/m and $\sigma_y = 73.709$ kN/m at $t = 3.16$ s. Both values were lower than the *tensile strengths* given in Table 7. Hence, the stability of the structure is guaranteed concerning the above-mentioned wind load.

6. Conclusions and outlook

A coupled algorithm for the numerical simulation of fluid–structure interactions was presented and the corresponding computer programs described. Both disciplines employ separate highly adapted codes being coupled by a neutral coupling interface. A *partitioned* but *fully implicit* coupling algorithm applies both programs for predicting fluid–structure interactions.

The present study involved two main test cases. First, the coupled code was applied to an academic fluid–structure configuration consisting of the laminar flow around several flexible L-shaped plates. Three characteristic wake regimes

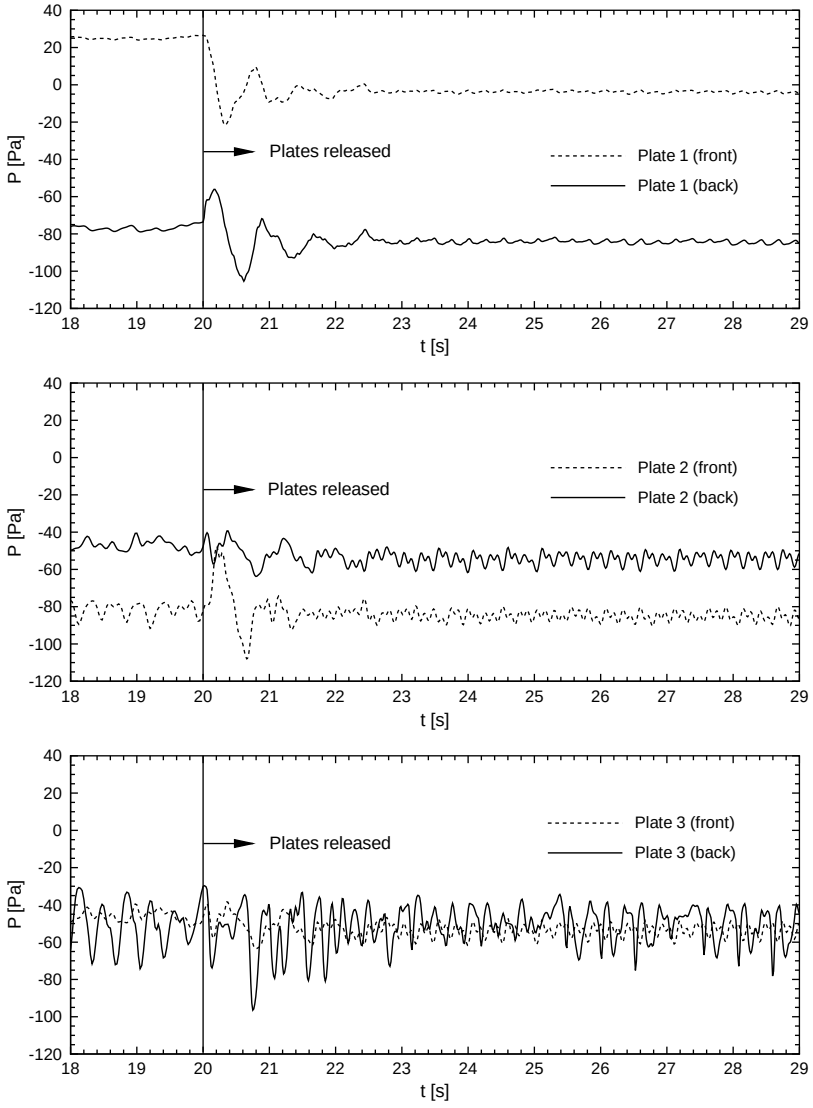

Fig. 30. Time history of the pressure at point V on the *front* side (*thin*, *dashed* curve) and on the *back* side (*thick*, *solid* curve) of the 1st plate (top), 2nd plate (middle), and 3rd plate (bottom) at $\mathrm{Re} = 500$ and $U_\infty = 16$ m/s.

were investigated (at Reynolds numbers 50, 200, and 500), leading to different structural responses, including resonance phenomena occurring when the vortex-shedding frequency is equal to an eigenfrequency of the plate. Furthermore, the mutual influence of two and three plates in a row behind each other was studied.

The second test case dealt with a real-life lightweight structure. A membranous roof in front of an office building was loaded by a combination of a basic flow and a temporary wind gust. Therefore, the contrasting features between the two cases were not only academia versus practice but also plate structure vs membrane.

All simulations showed stable convergent behavior even without any under-relaxation in the outer FSI iterations. The *convergence criteria* for the residual structural displacements referring to the maximum amplitude of oscillation were between 2×10^{-4} and 10×10^{-4} for the L-shaped plates and 7×10^{-4} for the membranous roof. In order to fall below these thresholds within each time step, one or two FSI iterations were required at the L-shaped plates. In the case of the tent roof, 2–15 FSI iterations were necessary owing to the membranous structure, which is much more flexible than the plate structure. Because of the great lack of experiments concerning flow-induced oscillations of simple structures, a comparison between numerical and measurement data was unfortunately not possible.

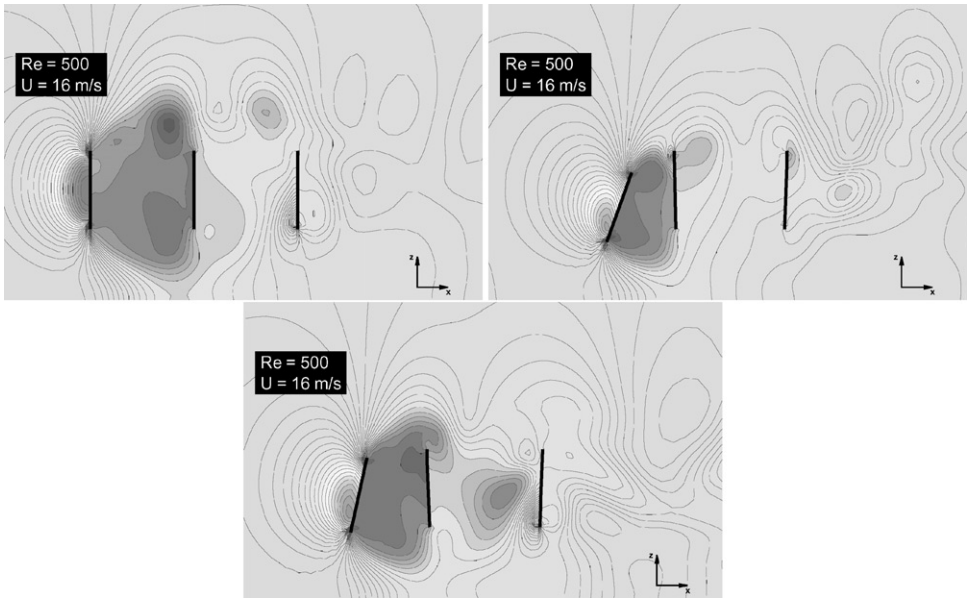

Fig. 31. Vertical cutting plane through the pressure field at $y = 0.92L$ (sketched in Fig. 29) for $\mathrm{Re} = 500$ and $U_\infty = 16$ m/s: $t = 19.5$ s—before the plates became flexible (top left), $t = 20.405$ s—largest distortions of the plates (top right), $t = 29$ s (bottom). The horizontal line at the bottom represents the ground at $z = 0$.

Fig. 32. Geometry of the membranous roof.

The state-of-the-art of the presented software package is the following: in principle, the algorithm is able to take into account time-dependent fluid–structure interactions, turbulent fluid flow, geometrically nonlinear displacements and nonlinear material behavior concerning thin shell and membrane structures. However, time-dependent turbulent flows around moving structures, where separation occurs, cannot yet be solved satisfactorily because of

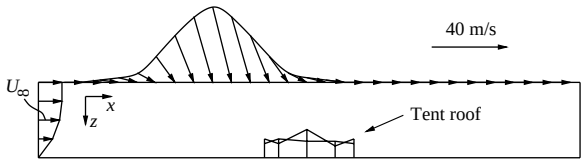

Fig. 33. Illustration of the inflow velocity $\mathbf{U}_{\text{inflow}}(x, z)$ at time $t = t_m = 3$ s with velocity reference vector (to scale).

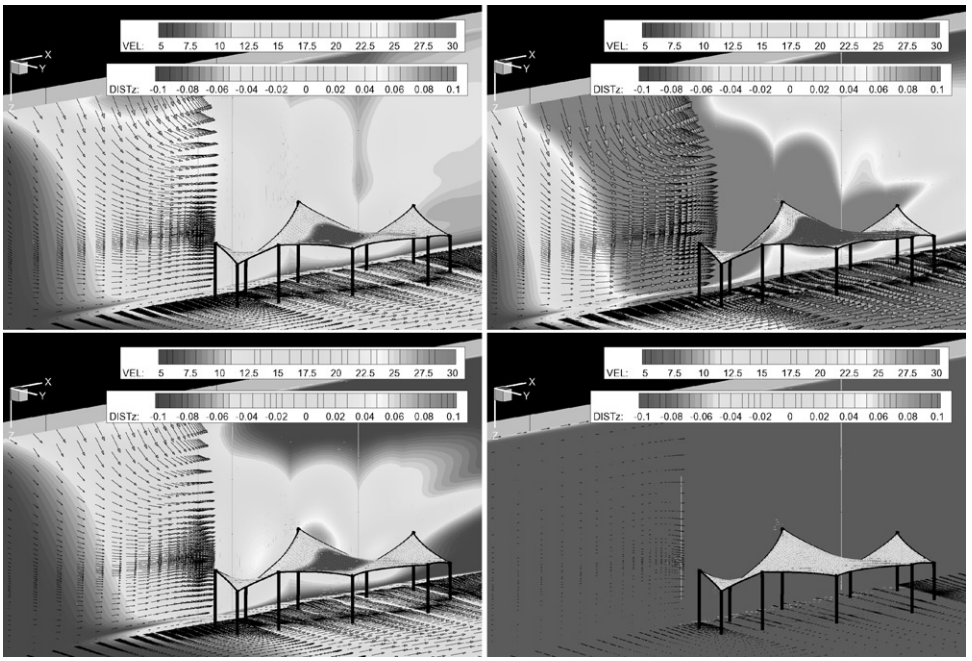

Fig. 34. Velocity distributions displayed near the horizontal wall (ground) and the vertical wall (office building behind the membranous roof) and displacements displayed on the roof surface at four different time steps: $t_1 = 2.0$ s (top left), $t_2 = 3.0$ s (top right), $t_3 = 4.2$ s (bottom left), $t_4 = 6.4$ s (bottom right).

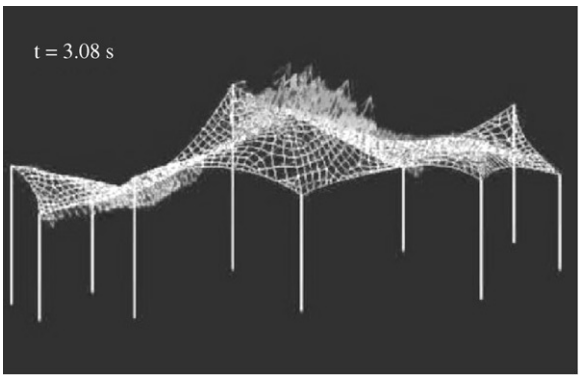

Fig. 35. Fluid loads at the CSD grid nodes for $t = 3.08$ s (displacements multiplied by a factor of 6).

the known weaknesses of the available turbulence models of k–ε type. Therefore, the CFD code *FASTEST-3D* is to be extended to *large eddy simulation* in the near future in order to reach higher Reynolds numbers, which are of real practical interest.

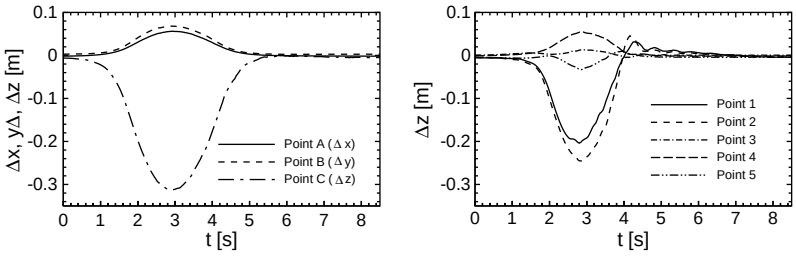

Fig. 36. Maximum displacements according to each of the Cartesian coordinates (left) and displacements in z direction at the evaluation points in Fig. 2 (right).

Table 7
Technical data for the membranous roof

Length	24.00 m
Width	3.00–8.50 m
Height	2.76–7.27 m
Total roof area	approx. 137 m^2
Membrane	PVC-coated polyester fabric
Thickness	$d = 0.8$ mm
Moduli of elasticity	$E_{warp} = 500$ MN/m^2
	$E_{weft} = 375$ MN/m^2
Shear modulus	$G = 12.5$ MN/m^2
Poisson's ratio	$v = 0.25$
Tensile strengths	$\sigma_{max,warp} = 115$ kN/m
	$\sigma_{max,weft} = 102$ kN/m
Specific weight	$m = 1.05$ kg/m^2
Pre-tension of the cables	$F_{pre,c} = 30$ kN
Pre-tension of the membrane	$F_{pre,m} = 3$ kN/m

Concerning the structural simulation part, the system architecture should be supplemented by a simulation code using *three-dimensional* finite element formulations instead of dimensionally reduced models such as shells and membranes.

Acknowledgements

Financial support by the Bayerische Forschungsstiftung in the Bavarian Network of Competence for High-Performance Scientific Computing (KONWIHR) is gratefully acknowledged. The authors also thank Dr. J. Bellmann and Dr. C. Katz of SOFiSTiK AG, Munich (Germany), for technical support and many useful discussions. All simulations were carried out on the SMP cluster *Hitachi SR8000-F1* at the Leibniz Computing Center, Munich (Germany). This support is also gratefully acknowledged. Cand.-Ing. C. Binder performed some of the calculations described in Section 4 during his student research project. His contribution is also gratefully acknowledged.

References

Ahrem, R., Hackenberg, M.G., Post, P., Redler, R., Roggenbuck, J., 2000. MpCCI—Mesh Based Parallel Code Coupling Interface. Institute for Algorithms and Scientific Computing (SCAI), GMD, http://www.mpcci.org/.

Bathe, K.-J., 1982. Finite Element Procedures in Engineering Analysis. Prentice-Hall Inc., Englewood Cliffs, NJ.

Bathe, K.J., Zhang, H., Wang, M.H., 1995. Finite element analysis of incompressible and compressible fluid flows with free surfaces and structural interactions. Computers and Structures 56 (2/3), 193–213.

Bellmann, J., 1998. Membrantragwerke und Seifenhaut—Unterschiede in der Formfindung. Bauingenieur 3 (98), 118–123.

Bergermann, R., Göppert, K., Schlaich, J., 1995. Die Membranüberdachungen für das Gottlieb-Daimler-Stadion, Stuttgart und den Gerry Weber Centre Court, Halle (Westfalen). Bauingenieur 70, 251–260.

Binder, C., 2001. Numerische Simulation der instationären Fluid-Struktur-Interaktion an einer flexiblen Winkelplatte. Studienarbeit, Lehrstuhl für Strömungsmechanik, Universität Erlangen-Nürnberg.

Brehm, M., Bader, R., Ebner, R., 2001. Höchstleistungsrechner in Bayern (HLRB): The Hitachi SR 8000-F1. http://www.lrz-muenchen.de/services/compute/hlrb/.

Breuer, M., 2002. Direkte Numerische Simulation und Large-Eddy Simulation turbulenter Strömungen auf Hochleistungsrechnern. Habilitationsschrift, Universität Erlangen-Nürnberg, Berichte aus der Strömungstechnik, ISBN: 3-8265-9958-6, Shaker Verlag, Aachen.

Bungartz, H.-J., Griebel, M., Zenger, C., 1996. Einführung in die Computergrafik—Grundlagen, Geometrische Modellierung, Algorithmen. Vieweg, Braunschweig/Wiesbaden.

Bungartz, H.-J., Frank, A., Meier, F., Neunhoeffer, T., Schulte, S., 1998. Fluid–structure interaction: 3D numerical simulation and visualization of a micropump. In: Friedrich, R., Bontoux, P. (Eds.), Computation and Visualization of 3D Vortical and Turbulent Flows, Notes on Numerical Fluid Mechanics, Vol. 64. Vieweg, Braunschweig/Wiesbaden, pp. 350–368.

Cebral, J.R., 1996. Loose coupling algorithms for fluid–structure interaction. Dissertation, George Mason University, Fairfax, VA.

Corney, J., 1997. 3D Modeling with the ACIS Kernel and Toolkit. Wiley, New York.

Demirdžić, I., Perić, M., 1990. Finite volume method for prediction of fluid flow in arbitrarily shaped domains with moving boundaries. International Journal for Numerical Methods in Fluids 10, 771–790.

Durst, F., Schäfer, M., 1996. A parallel block-structured multigrid method for the prediction of incompressible flows. International Journal for Numerical Methods in Fluids 22, 549–565.

Dütsch, H., Melling, A., Durst, F., 1999. Coupled Numerical Computations of the Fluid Damped Oscillations of a Lamina. Lecture Notes in Computational Science and Engineering, Vol. 8. Springer, Heidelberg, pp. 103–112.

Farhat, C., Lesionne, M., Le Tallec, P., 1998. Load and motion transfer algorithms for fluid/structure interaction problems with non-matching discrete interfaces: momentum and energy conservation, optimal discretization and application to aeroelasticity. Computational Methods in Applied Mechanical Engineering 157, 95–114.

Ferziger, J.H., Perić, M., 1999. Computational Methods for Fluid Dynamics, 2nd Edition. Springer, Berlin, Heidelberg, New York.

Frandsen, J.B., 1999. Computational fluid–structure interaction applied to long-span bridge design. Ph.D. Thesis, Department of Engineering, Cambridge University, UK.

Glück, M., Breuer, M., Durst, F., Halfmann, A., Rank, E., 2001. Computation of fluid–structure interaction on lightweight structures. Journal of Wind Engineering and Industrial Aerodynamics 89 (14–15), 1351–1368.

Katz, C., Bellmann, J., 1995a. ASE-Handbuch. SOFiSTiK GmbH, Katz + Bellmann, Munich.

Katz, C., Bellmann, J., 1995b. DYNA-Handbuch. SOFiSTiK GmbH, Katz + Bellmann, Munich.

Kovacs, I., 1994. Synthetic Wind for Investigation in Time-Domain. ASCE, Structures Congress, Atlanta, GA.

Lesoinne, M., Farhat, C., 1998. Improved staggered algorithms for the serial and parallel solution of three-dimensional nonlinear transient aeroelastic problems. In: Idelsohn, S., Onate, E., Dvorkin, E. (Eds.), Computational Mechanics—New Trends and Applications. CIMNE, Barcelona.

Le Tallec, P., Mouro, J., 1998. Fluid–structure interaction with large structural displacements. Computational Fluid Dynamics. ECCOMAS 1998, John Wiley & Sons, New York, pp. 1032–1039.

Mok, D.P., Wall, W.A., 2001. Partitioned analysis schemes for the transient interaction of incompressible flows and nonlinear flexible structures. In: Wall, W.A., Bletzinger, K.-U., Schweizerhof, K. (Eds.), Trends in Computational Structural Mechanics. CIMNE, Barcelona.

MPI, 2001. http://www-unix.mcs.anl.gov/mpi/.

Pedley, T.J., Stephanoff, K.D., 1985. Flow along a channel with a time-dependent indentation in one wall: the generation of vorticity waves. Journal of Fluid Mechanics 160, 337–367.

Ralph, M.E., Pedley, T.J., 1988. Flow in a channel with a moving indentation. Journal of Fluid Mechanics 190, 87–112.

Rank, E., Halfmann, A., Rücker, M., Katz, C., Gebhard, S., 2000. Integrierte Modellierungs- und Berechnungssoftware für den konstruktiven Ingenieurbau: Systemarchitektur und Netzgenerierung. Bauingenieur 75, 60–66.

Steindorf, J., Matthies, H.G., 1999. Efficient partitioned methods for the computation of fluid–structure interaction on parallel computers. Proceedings of the Third Euro-Conference on Parallel and Distributed Computing for Computational Mechanics. Civil-Comp Press, Edinburgh.

Thompson, J.F., Warsi, Z.U.A., Wayne Mastin, C., 1985. Numerical Grid Generation. North-Holland, New York, Amsterdam, Oxford.

Wall, W.A., 1999. Fluid–Struktur-Interaktion mit stabilisierten Finiten Elementen. Dissertation, Institut für Baustatik, Universität Stuttgart.

Wall, W.A., Mok, D.P., Ramm, E. 1999. Partitioned analysis approach for the transient, coupled response of viscous fluids and flexible structures. Proceedings of the ECCM Solids, Structures and Coupled Problems in Engineering, Munich, Germany.

Wall, W.A., Mok, D.P., Ramm, E., 2000. Simulation of nonlinear shells interacting with instationary flows. Proceedings of Fourth International Colloquium on Computation of Shell & Spatial Structures, June 4–7, Chania, Crete, Greece.

Zahlten, W., 1998. Zur numerischen Simulation winderregter Strukturen. Habilitationsschrift, Fakultät für Bauingenieur- und Vermessungswesen, RWTH, Aachen.

Zienkiewicz, O.C., Taylor, R.L., 1991. The Finite Element Method, Vol. 2, 5th Edition. Butterworth-Heinemann, Oxford.